JAMES | Journal of Advances in Modeling Earth Systems

RESEARCH ARTICLE
10.1029/2019MS001698

Self-Aggregation of Convection in Spatially Varying Sea Surface Temperatures

Sebastian K. Müller[1] and Cathy Hohenegger[1]

[1]Max Planck Institute for Meteorology, Hamburg, Germany

Key Points:
- A convergence line, forced by an SST contrast and comprising deep convection, is unstable to the self-aggregation of convection
- The zonally elongated convective clusters export moisture only meridionally and only between 1 and 5 km height

Correspondence to:
S. K. Müller,
sebastian.mueller@mpimet.mpg.de

Citation:
Müller, S. K., & Hohenegger, C. (2020). Self-aggregation of convection in spatially varying sea surface temperatures. *Journal of Advances in Modeling Earth Systems*, *12*, e2019MS001698. https://doi.org/10.1029/2019MS001698

Received 26 MAR 2019
Accepted 25 NOV 2019
Accepted article online 28 DEC 2019

Abstract The phenomenon of self-aggregation of convection was first identified in convection-permitting simulations of radiative convective equilibrium, characterized by homogeneous boundary conditions and in the absence of planetary rotation. In this study, we expose self-aggregation of convection to more complex, nonhomogeneous boundary conditions and investigate its interaction with convective aggregation, as forced by large-scale variations in sea surface temperatures (SSTs). We do this by conducting radiative convective equilibrium simulations on a spherical domain, with SST patterns that are zonally homogeneous but meridionally varying. Due to the meridional contrast in SST, a convergence line first forms, mimicking the Intertropical Convergence Zone. We nevertheless find that the convergence line breaks up and contracts zonally as a result of the self-aggregation of convection. The contraction is significant, being here more than 50% of the original extent. The stability of the convergence line is controlled by the strength of the meridional circulation, which depends upon the imposed SST contrast. However, the process of self-aggregation, once it is initiated, is insensitive to the strength of the SST contrast. The zonal contraction is accompanied by a slight meridional expansion and a moistening of the high latitudes, where SSTs are low. The moistening of the high latitudes can be understood from the fact that the convective cluster intensifies and expands its moist meridional low-level outflow when it self-aggregates zonally. Overall, our results suggest that the Intertropical Convergence Zone may be unstable to the self-aggregation of convection, that self-aggregation may serve as a precursor to the formation of atmospheric rivers, and that longer convergence lines are more likely to exist in regimes with strong SST gradients.

Plain Language Summary Storm clouds over the tropical oceans are found to organize in large systems. They tend to form where the temperatures of the sea surface (SSTs) are highest and that is most often along the equator. With idealized computer model experiments we investigate how different sea surface temperature patterns, along with the natural tendency of clouds to aggregate, control the properties of the storm cloud system. We find that a contrast in SSTs immediately acts to organize the storm clouds. In our simulations, this means the formation of a long line of clouds, oriented along the equator. With time however, this line breaks up and then contracts just by itself. Here we find that the spatial difference in SSTs controls the stability of the cloud system against the break up and contraction: The stronger the difference in SST, the more stable is the line of clouds. Also we find that the storm clouds export moisture only in one direction: from the equator to the higher latitudes.

1. Introduction

Convective aggregation, meaning the clustering of convective clouds, is a key element of tropical dynamics. It manifests itself in phenomena like the Intertropical Convergence Zone (ITCZ) and the Madden-Julian Oscillation and also plays a role in tropical cyclogenesis. Convection-permitting numerical modeling studies of radiative convective equilibrium (RCE) have shown that convective aggregation also occurs when boundary conditions and forcing, which are sea surface temperatures (SSTs) and insolation, are horizontally homogeneous and in the absence of rotation. It is then referred to as self-aggregation of convection (Bretherton et al., 2005).

The mechanisms leading to and maintaining self-aggregation of convection are diverse and may be summarized as the interaction of convection, moisture, radiation, and circulation (Wing et al., 2017): Longwave radiative cooling is stronger in areas with clear sky or in areas populated by shallow convection than in areas populated by deep convection. Through the resulting differential radiative cooling in the planetary boundary

layer, a shallow overturning circulation can form, which imports moist static energy up-gradient from the dry to the moist convecting region and leads to the self-aggregation of convection (Muller & Held, 2012; Muller & Bony, 2015). Further positive feedbacks that can promote self-aggregation include interactions between convection and surface fluxes (Tompkins & Craig, 1998; Wing & Emanuel, 2014), a coarsening of the moisture field (Craig & Mack, 2013; Tompkins, 2001), entrainment (Becker et al., 2017; Tompkins & Semie, 2017) and virtual effects of water vapor (Yang, 2018). However, the occurrence of self-aggregation and mechanisms at play appear to be sensitive to model properties, such as the grid spacing, domain size, and representation of convection (Muller & Held, 2012). To this end, the Radiative Convective Equilibrium Model Intercomparison Project (Wing et al., 2018) sets a standard for simulations of RCE and in doing so aims to clarify the mechanisms of self-aggregation of convection. Other interesting properties of self-aggregation of convection include its sensitivity to SST (Held et al., 1993; Wing & Emanuel, 2014), its potential effect on equilibrium climate sensitivity (*Iris effect*; Mauritsen & Stevens, 2015), and its impact on the stabilization of the climate (Bretherton et al., 2005; Hohenegger & Stevens, 2016).

The potential importance of the self-aggregation of convection for climate, at least in idealized studies, has motivated one of the guiding questions of the World Climate Research Programme Grand Challenge Initiative on Clouds, Circulation and Climate Sensitivity (Bony et al., 2015); that is, "what role does convective aggregation play in climate?" The RCE modeling framework nevertheless remains highly idealized, and findings might not be relevant to the real atmosphere, as stressed in Mapes (2016). External forcing such as spatially varying SSTs, large-scale low-level convergence of trade winds (Back & Bretherton, 2009; Bretherton & Sobel, 2002; Lindzen & Nigam, 1987), and wind shear (Rotunno et al., 1988), which are not considered in the RCE framework, are known to promote the organization of convection in the tropics and may mask the effects of self-aggregation. Consequently, observational evidence of self-aggregation of convection or of its expected effects on climate has been sought (Beucler et al., 2019; Holloway et al., 2017; Tobin et al., 2012), but the importance of self-aggregation of convection in the presence of external forcing remains unclear.

In this paper we add one step of complexity to the RCE framework and investigate how self-aggregation of convection is affected by the presence of an external forcing in the form of spatially varying SSTs. To that aim, we impose a large-scale SST pattern that only varies in the meridional direction and that is symmetric across the equator. On the one hand we expect the SST contrast to spin up a shallow circulation in the meridional direction, leading to the formation of a convergence line along the equator. On the other hand, in the zonal direction, where SSTs are homogeneous, self-aggregation and its accompanying shallow circulation may develop and act on the convergence line and on the SST-driven circulation.

With our experimental design we simulate tropical convection that is organized by both self-aggregation physics and SST patterns. The two processes act on different time scales and generate their own circulations that will interact and compete in determining the final spatial distribution of convection. Depending on the strength of the underlying circulations, one or the other, or a combination of both, may win. Such a competition between the self-aggregation of convection and its associated underlying circulation and an externally forced circulation was recently documented in Hohenegger and Stevens (2018) in the context of a self-aggregation study conducted over a land planet where the externally forced circulation resulted from soil moisture gradients. As such, our study will determine whether the spatial distribution of convection is determined by the aggregation of convection forced by the spatially varying SSTs and/or by the self-aggregation of convection, by focusing on an analysis of the flow field. Moreover, we will investigate how the interactions between the various circulations affect the spatial distribution of moisture.

In general, our study bridges the gap between traditional RCE studies and beta plane (Bretherton & Khairoutdinov, 2015; Nolan et al., 2010) and aqua-planet experiments (Neale & Hoskins, 2000b). Relevant related modeling approaches employing spatially nonuniform but prescribed boundary conditions are found in Raymond (1994), Grabowski (2001), and Tompkins (2001a). Furthermore, simulations of RCE on domains with a *channel* geometry (e.g. Posselt et al., 2012; Wing & Cronin, 2016) are of particular interest to this study. These simulations show a flatter and more realistic moisture distribution (Wing & Cronin, 2016).

Eventually, this study's simulations suggest a link of convective aggregation with the formation of atmospheric rivers. Atmospheric rivers are narrow, elongated, synoptic-scale streams, rich with water vapor (Gimeno et al., 2014; Newell et al., 1992). They account for the major fraction of the meridional global

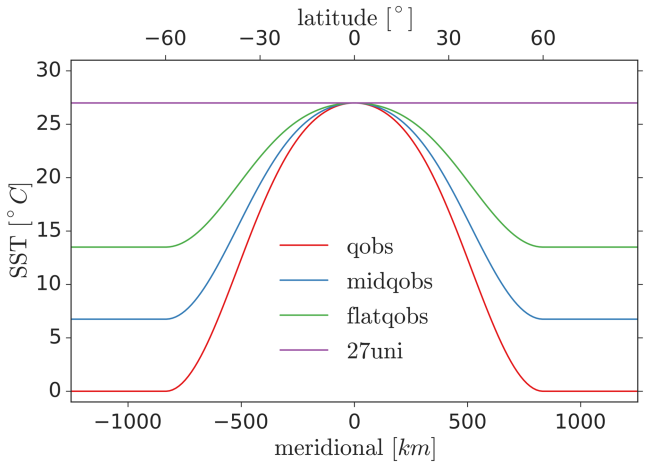

Figure 1. Zonally symmetric SST profiles characterizing the four simulations.

moisture transport (Zhu & Newell, 1998) and are associated with severe precipitation events (Eiras-Barca et al., 2018; Lavers et al., 2012; Ralph et al., 2010). Atmospheric rivers have been studied in observations (Ralph et al., 2004), reanalysis data (Guan & Waliser, 2015), and numerical experiments (Jankov et al., 2009; Swenson et al., 2018).

The paper is organized as follows. In section 2 we introduce the numerical model and the SST patterns used for our set of four simulations. In section 3 we first describe the convective evolution (section 3.1). Second, we quantify and investigate the effect of spatially varying SSTs on the self-aggregation of convection (section 3.2) by looking into moisture variance, circulation, and cloud cluster geometry. Although the aggregation of convection is confined within the tropics, it has unique implications for the moisture budget of the high latitudes in comparison to traditional RCE or aqua-planet simulations. This unique feature will be examined and explained in section 3.3 by analyzing the moisture import and export of the cloud cluster. Finally, conclusions are presented in section 4.

2. Methods

We use an idealized numerical model of the tropical atmosphere, the ICON-Spherical Limited Area Model (Müller, 2019; Müller et al., 2018). The model is based upon the atmospheric component of the ICOsahedral Non-hydrostatic atmosphere model, ICON-A (Giorgetta et al., 2018).

In this model setup we use a spherical domain with a radius 1/8 of that of the Earth, resulting in a circumference of 5,004 km. The horizontal grid spacing is 2.5 km and thus may be classified as convection permitting (Prein et al., 2015). The vertical grid has 75 levels and a model top at 30 km. It is stretched with grid spacings ranging from 65 m, between the lowest levels, to about 500 m at 15 km. A Rayleigh damping layer (Klemp et al., 2008) acts above 25 km to prevent wave reflection. The simulations are integrated and analyzed for a period of 120 days. Given the employed horizontal grid spacing, the convection scheme, the subgrid cloud cover scheme, and the gravity wave drags are turned off. The remaining physical parameterizations (radiation, microphysics, and diffusion) are as in Giorgetta et al. (2018).

Following the setup of past RCE experiments, we use a water-covered surface, there is no rotation, and the insolation is spatially uniform. Following Popke et al. (2013), the insolation varies diurnally and is on average 340.2 W/m^2. The SST is prescribed as the bottom boundary condition and is invariant in time. Temperature and pressure fields are initialized following Jablonowski and Williamson (2006), but with the winds set to zero. Also, humidity is set to be spatially uniform over the domain, with an exponentially decaying vertical profile and a water vapor path of 25 mm. For the initialization humidity and temperature are slightly altered with random white noise added at the lowest model levels.

To investigate the effect of spatially varying SSTs on the self-aggregation of convection, we conduct four different sensitivity experiments with SST profiles as shown in Figure 1. One simulation (27 uni) has uniform SSTs of 27 ° C, mimicking a typical three-dimensional model of RCE (Bretherton et al., 2005). The other three experiments use SST profiles that are zonally symmetric but meridionally varying and are described by equation (1). The profiles are the "qobs"-SST profile, as originally defined by Neale & Hoskins (2000a, 2000b) for the aqua-planet experimental protocol and variations thereof: "midqobs" and "flatqobs." All SST profiles have a maximum SST, SST^{max}, of 27 ° C at the equator and decrease to a minimum SST, SST^{min}, of 0 ° C (qobs), 6.25 ° C (midqobs), and 13.5 ° C (flatqobs) for latitudes poleward of 60°. Per construction, the three SST profiles only differ in their meridional contrast (SST^{max}-SST^{min}) with values of 27, 20.75, and 13.5 °C for qobs, midqobs, and flatqobs, respectively. Hence, in the remainder of the text, the term SST contrast is used to refer to these experiments and to the effects of spatially varying SSTs on the self-aggregation of convection. Changing the SST contrast is expected to alter the strength of the SST-forced circulation, thus affecting the strength of the external forcing on convection and the likelihood for self-aggregation to develop. Note that, even though we use the qobs profile as traditionally employed in aqua-planet experiments, the use of a smaller planet radius implies a much stronger SST gradient in our simulation. Bechtold et al. (2013) also used the qobs profile in their small planet experiment but nevertheless obtained a similar latitudinal ITCZ

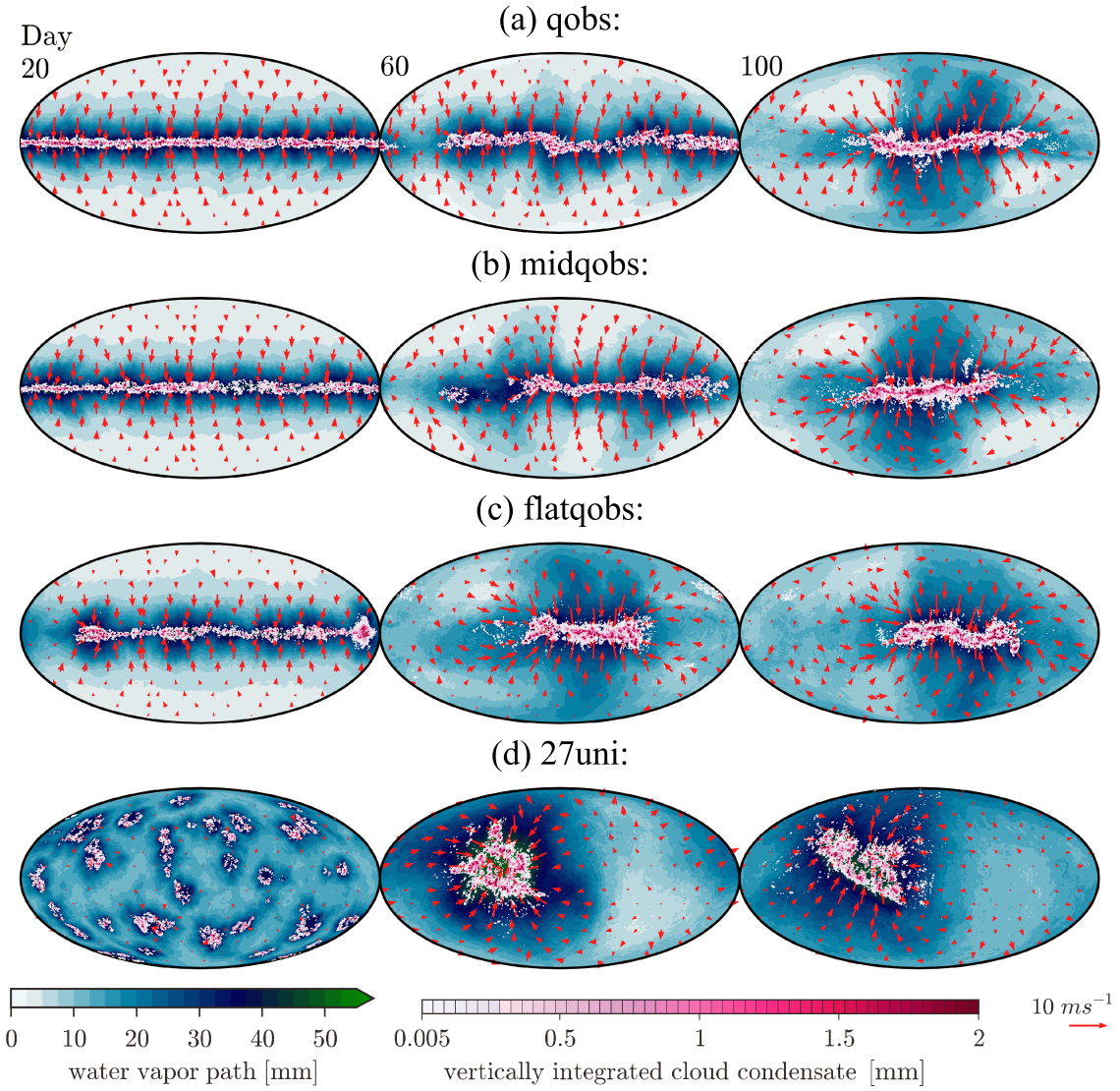

Figure 2. Daily means of vertically integrated cloud condensate [mm] (white to pink contours), water vapor path [mm] (shading) and surface flow (red arrows).

width as in their full aqua-planet experiment (see their Figure 3). In addition and as indicated in section 1, the relevant parameter is the strength of the underlying circulation spun up by the SST contrasts. With zonal average values of about 4 to 6 m/s close to the equator (see, e.g., Figure 2), the values are similar and if anything rather smaller than the values obtained in traditional aqua-planet experiments (see e.g. Figure 3 in Möbis & Stevens, 2012).

$$\text{SST} \quad (\phi) = \begin{cases} \text{SST}^{\min} + (\text{SST}^{\max} - \text{SST}^{\min}) \frac{(1-\sin(\frac{3}{2}\phi)^2)+(1-\sin(\frac{3}{2}\phi)^4)}{2}, & \text{if} -\frac{\pi}{3} < \phi < \frac{\pi}{3} \\ \text{SST}^{\min}, & \text{if} \phi \le -\frac{\pi}{3} \vee \phi \ge \frac{\pi}{3} \end{cases}. \tag{1}$$

3. Results

3.1. Overview of the Convective Evolution

In Figure 2 we introduce the convective evolution in the four simulations, as illustrated by the cloud water path, the water vapor path (prw), and by the surface flow.

The experiment 27 uni, characterized by uniform SSTs, shows the typical evolution of past convection-permitting three-dimensional simulations of RCE conducted in a square domain: At first, individual convective clouds appear randomly distributed. With time the clouds merge and form larger-scale convective systems. Ultimately, a single approximately circular convective cloud cluster remains, within an area of high

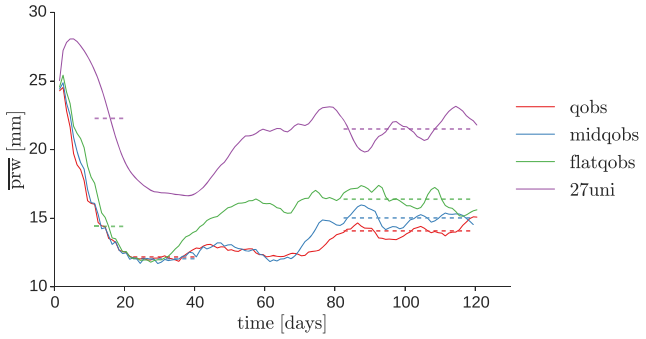

Figure 3. Temporal evolution of the daily mean and domain-mean water vapor path (prw; mm). Dashed lines denote the averages for the quasi-equilibrium period P_{quasi} and for the equilibrium period P_{equi}; see Table 1 for the definition of the time periods.

moisture content and surrounded by a dry nonconvecting region. The low-level branch of the deep overturning circulation is at all times directed from the dry to the moist regions, with ascent in moist convection, and outflow at the top of the deep convection. The outflow spreads toward and subsides in the dry region maintaining a strong capping inversion. The resulting strong drying prevents the development of clouds in the subsiding region as observed in past RCE simulations. The simulation reaches its RCE after about 60 days (see, e.g., Figure 2).

In contrast, the three simulations with spatially varying SSTs first form a continuous convergence line (see Day 20), which is located along the equator where SSTs peak. The distribution of clouds and precipitation in the tropics are reminiscent of their distribution in traditional aqua-planet experiments that use a zonally varying insolation and rotation (see, e.g., Möbis & Stevens, 2012). Also, the strength of the meridional overturning circulation is comparable to the one in aqua-planet experiments (Müller, 2019). The low-level flow is purely meridional and directed equatorward, thereby constraining the occurrence of convection to the convergence line along the equator. Elsewhere, the atmosphere is cloud-free and dry, both due to the absence of low-level convergence, low SSTs, and radiative cooling of the lowest model levels.

However, at the latest by Day 60, the overall flow pattern and the geometry of the convergence line change. The convergence line does not span the equator anymore. This happens as the convergence line breaks up and contracts in the zonal direction. In agreement with these changes, the surface circulation develops a zonal component. Still, clouds and precipitation remain confined to the equatorial region.

Given this evolution, we identify the initial formation of the convergence line as the aggregation of convection forced by the SST contrast and will refer to it simply as forced aggregation of convection in the remaining text. In contrast, we identify the breakup and the contraction of the convergence line in the zonal direction as self-aggregation of convection, since it happens above zonally homogeneous SSTs. Finally, we will use the term convective aggregation as a generic term without specific reference to forced aggregation of convection or to self-aggregation of convection. We will quantify and investigate in detail the interplay between forced aggregation of convection and self-aggregation of convection in section 3.2.

Figure 3 shows the temporal evolution of the domain-mean water vapor path given its tight relationship to convection, precipitation, and self-aggregation. All simulations are initialized with the same thermodynamic profiles and a horizontally homogeneous moisture distribution that results in a water vapor path of 25 mm. As expected from past RCE studies, the self-aggregation of convection in 27 uni leads to a drying of the atmosphere until Day 40. Once one convective cluster has formed (on Day 50), the water vapor path increases again until it reaches its equilibrium value. Although the experiments with SST contrasts exhibit a similar evolution of the water vapor path, the causes are different. In those experiments, the initial drying is associated with the forced aggregation of convection, whereas the subsequent moistening is the result of the self-aggregation of convection. In that context, a unique feature of the three simulations with SST contrasts, which has not been observed in traditional RCE experiments, is the moistening of the high-latitude areas (see Figure 2). This moistening is not symmetric around the cloud cluster, as in 27 uni, but predominantly in the meridional direction. Given this unique character, the influence of forced aggregation of convection and self-aggregation of convection on the moisture evolution will be investigated in detail in section 3.3.

3.2. Convective Aggregation in the Tropics

From the convective evolution described previously, it became evident that in all the simulations the convective clouds aggregate to form a single large-scale cloud cluster, which in its equilibrium state does not span the full equator in the simulations with SST contrasts. We analyze this behavior in this section in detail, first by looking into measures of convective aggregation and then by explaining this behavior based on the competition between the circulation forced by the spatially varying SST and the circulation associated with the self-aggregation. Finally, we quantify the effects of forced aggregation and self-aggregation on the cluster geometry.

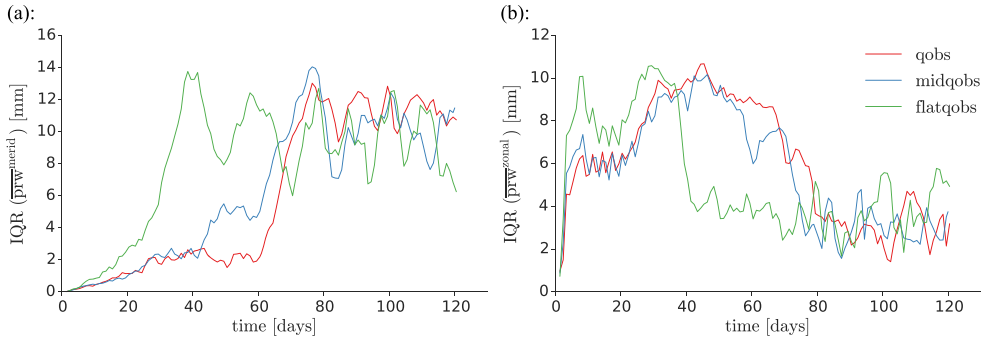

Figure 4. Temporal evolution of the interquartile range (IQR) of the daily mean of the (a) meridional mean (IQR($\overline{\text{prw}}^{\text{merid}}$)) and (b) zonal mean (IQR($\overline{\text{prw}}^{\text{zonal}}$)) of the water vapor path (mm).

3.2.1. Quantification of Aggregation Through Moisture Variance

A common measure of self-aggregation of convection is the spatial variance of the water vapor path (e.g., Holloway & Woolnough, 2016; Muller & Held, 2012). We use here the interquartile range (IQR), which is the 75th minus the 25th percentile of the distribution. The self-aggregation of convection typically reveals itself by high moisture variance due to the formation of a single cloud cluster located within a moist region in an otherwise extremely dry and nonconvecting domain. The associated overturning circulation promotes both the moistening of the cluster and the drying of the nonconvecting region through large-scale subsidence. However, we aim here to isolate two distinct types of convective aggregation, namely, forced aggregation and self-aggregation. To isolate these two types of aggregation, we assume that forced aggregation dominates in the meridional direction due to the presence of the SST contrasts, whereas self-aggregation dominates in the zonal direction where the SST is spatially uniform. We thus slightly adapt the IQR measure by applying it selectively to the zonal mean of the water path and to the meridional mean of the water path.

In Figure 4a the IQR of the meridional mean of the water vapor path, denoted as IQR($\overline{\text{prw}}^{\text{merid}}$), is shown. It is computed by taking the meridional average of the daily mean values of the water vapor path, before computing their IQR as a function of longitude. IQR($\overline{\text{prw}}^{\text{merid}}$) is a measure of zonal self-aggregation of convection exclusively. For as long as the convergence line is continuous, this variance remains small (<3 mm). However, as soon as the convergence line breaks up, the measure of zonal self-aggregation increases rapidly. This happens after about 20 days for flatqobs and after about 60 days for qobs. For midqobs we note that the slight increase of IQR($\overline{\text{prw}}^{\text{merid}}$) at day 40 results from the convergence line first breaking at two locations. The two clusters then merge again, before starting to zonally contract around Day 60.

Figure 4 shows clearly that the imposed SST contrast controls the onset of self-aggregation. Even though some randomness in the actual onset time of self-aggregation can be expected, Figure 4 displays a systematic relationship between the SST contrast and the onset of self-aggregation: The larger the SST contrast is, the longer it takes for the convergence line to break up and for self-aggregation to occur. However, after self-aggregation has begun, its pace, measured by the rate of change with time of IQR($\overline{\text{prw}}^{\text{merid}}$), is equal for the three SST contrast experiments. This can be seen by the three curves in Figure 4a being parallel once self-aggregation has set in. This means that the strength of the SST contrast controls the stability of the convergence line but has little effect on the pace of self-aggregation. This makes sense as all the three simulations exhibit similar SSTs along the equator where self-aggregation takes place.

In Figure 4b the IQR of the zonal mean of the water vapor path, denoted IQR($\overline{\text{prw}}^{\text{zonal}}$), is shown. It is a measure of meridionally forced aggregation of convection only. Here, the SST contrast immediately forces the meridional aggregation and leads to an increase in IQR in agreement with the formation of the convergence line. Just before the convergence line begins to break up, the meridional aggregation peaks. Remarkably, IQR($\overline{\text{prw}}^{\text{zonal}}$) drops significantly thereafter. In section 3.3, we will demonstrate that this is a consequence of moisture export to higher latitudes by the aggregated cluster.

Based on these considerations and to help further the analysis of the simulations in sections 3.2.2, 3.2.3, and 3.3, we define three characteristic periods in the evolution of the convective system: P_{quasi}, P_{trans}, and P_{equi}. P_{quasi} refers to the quasi-stable state of the system as controlled by forced aggregation, when the convergence line spans the equator. P_{trans} is a purely transient state during which the convergence line contracts

Table 1
Summary of Various Properties (Temporal Mean ± Standard Deviation) of the Simulations and of Their Cloud Clusters, for the Characteristic Periods P

	SST contrast experiments						
	qobs		midqobs		flatqobs		27 uni
Type of period [start day, end day]	P_{quasi} [21, 40]	P_{equi} [81, 120]	P_{quasi} [21, 40]	P_{equi} [81, 120]	P_{quasi} [11, 20]	P_{equi} [81, 120]	P_{equi} [71, 120]
Cluster zonal extent [km]	5,002 ± 9	2,307 ± 198	4,996 ± 20	2,114 ± 363	4,672 ± 300	1,697 ± 271	—
Cluster meridional extent [km]	348 ± 28	441 ± 46	335 ± 29	522 ± 80	375 ± 31	642 ± 62	—
Cluster circumference [km]	11,463 ± 159	5,788 ± 457	11,502 ± 227	5,659 ± 706	11,967 ± 1384	4,342 ± 610	6,365 ± 995
Cluster area fraction [−]	0.12 ± 0.008	0.07 ± 0.005	0.12 ± 0.004	0.07 ± 0.010	0.11 ± 0.018	0.07 ± 0.008	0.20 ± 0.046
A_{imp}/A_{exp} [−]	3.1 ± 0.3	3.1 ± 0.4	3.4 ± 0.4	3.0 ± 0.5	4.8 ± 1.0	3.2 ± 0.6	4.6 ± 1.3
$\overline{prw}$ [mm]	12.2 ± 0.3	14.1 ± 0.4	12.1 ± 0.2	15.0 ± 0.5	14.4 ± 1.6	16.4 ± 0.7	21.8 ± 0.9
$\overline{pr}$ [mm/day]	2.7 ± 0.2	3.1 ± 0.2	2.7 ± 0.2	3.1 ± 0.3	2.9 ± 0.5	3.1 ± 0.4	3.2 ± 0.6
$\overline{\lvert u_{sfc}\rvert}$ [m/s]	0.53 ± 0.06	1.65 ± 0.15	0.54 ± 0.06	1.63 ± 0.16	0.54 ± 0.06	1.66 ± 0.11	—
$\overline{\lvert v_{sfc}\rvert}$ [m/s]	3.37 ± 0.08	2.94 ± 0.11	3.07 ± 0.12	2.64 ± 0.13	2.58 ± 0.18	2.28 ± 0.14	—
$\overline{wdsp_{sfc}}$ [m/s]	3.41 ± 0.08	3.38 ± 0.10	3.11 ± 0.12	3.11 ± 0.15	2.64 ± 0.17	2.82 ± 0.15	2.1 ± 0.29

Note. The quasi-equilibrium period P_{equi} before self-aggregation sets in, the transient period P_{trans} during self-aggregation, and the equilibrium period P_{equi}; see text for more details on the definition. A_{imp}/A_{exp} (−) is the ratio of the clusters' importing to exporting integrated moisture flux, $\overline{prw}$ (mm) the domain-mean water vapor path, $\overline{pr}$ (mm/day) the domain-mean precipitation flux, and $\overline{wdsp_{sfc}}$ the domain-mean surface wind speed, whereas $\overline{\lvert u_{sfc}\rvert}$ and $\overline{\lvert v_{sfc}\rvert}$ (m/s) are the domain means of the absolute magnitude of the zonal and meridional wind components.

zonally through the action of self-aggregation. Finally, P_{equi} is the equilibrium state. The three distinct periods are derived visually from the distribution of clouds, like shown in Figure 2 and from Figure 4. More specifically, P_{quasi} terminates at the onset of self-aggregation. For qobs and midqobs periods of 20 days were identified. Considering the fact that for flatqobs self-aggregation sets in so early, we defined P_{quasi} for a shorter period of only 10 days. Also note that some of the investigated variables, particularly $\overline{prw}$ and IQR($\overline{prw}^{merid}$), are already changing during those 10 days. P_{trans} is given by the onset time and completion of self-aggregation. For P_{equi}, we chose the last 40 days for SST contrast experiments and the last 50 days for 27 uni. The days making up the different periods are indicated in Table 1.

3.2.2. Analysis of the Circulations

To understand the previously described interactions between forced aggregation and self-aggregation of convection, we look into the associated meridional and zonal overturning circulations and focus on their surface components.

On the one hand, from previous RCE studies (e.g., Coppin & Bony, 2015) and as found in 27 uni, we know that the self-aggregation of convection is associated with a circulation whose low-level branch is directed from the nonconvective to the convective regions. In our SST contrast simulations, such a circulation would first manifest itself in the zonal direction with an expected zonal wind velocity component directed toward the convective cluster at the surface. On the other hand, differential surface heating, as here induced by the spatial SST variations, can also spin up a circulation. Here the surface component of the circulation should be directed from the region of low SST to the region of high SST (Back & Bretherton, 2009; Lindzen & Nigam, 1987). In our simulations, such a circulation would predominantly manifest itself in the meridional direction with a strength depending upon the imposed SST contrast and a meridional wind velocity component at the surface directed from the high latitude toward the equator. In the following paragraphs we diagnose the strength of these two circulations and their interactions.

In Figure 5, the day and domain means of the absolute magnitude of the zonal and meridional wind components at the surface, $\overline{|u_{sfc}|}$ and $\overline{|v_{sfc}|}$, are shown. Note that we here take the absolute magnitude first, before computing the temporal and spatial means, so that the circulations north and south and east and west of the cluster do not cancel out.

For as long as the convergence line spans the equator, the magnitude of $\overline{|u_{sfc}|}$ is only around 0.5 m/s. It represents the signature of cold pools and confirms that the circulation is indeed predominantly oriented in the meridional direction in agreement with the meridional SST contrast (see also Figure 2). However, as soon as zonal self-aggregation sets in, a zonal circulation emerges and manifests itself by an increase of $\overline{|u_{sfc}|}$. Importantly, the rate of change of $\overline{|u_{sfc}|}$ is similar for the different SST contrasts. This is reminiscent and

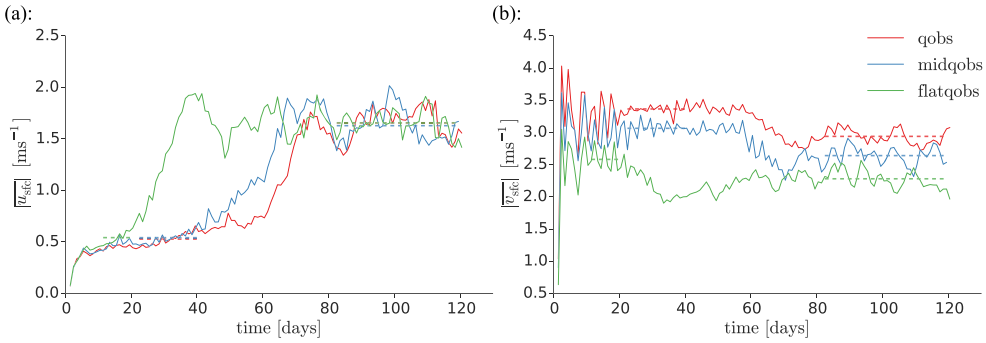

Figure 5. Temporal evolution of the daily mean and domain mean of the absolute value of the (a) zonal ($\overline{|u_{sfc}|}$) and (b) meridional ($\overline{|v_{sfc}|}$) wind components. Dashed lines denote the averages for the periods P_{quasi} and P_{equi}.

consistent with the similar pace of self-aggregation in the evolution of IQR($\overline{prw}^{merid}$) (see Figure 4) where the rate of change was also about the same for all three SST profiles. Eventually, for all three SST contrast experiments, the strength of the zonal circulation, as estimated from the mean of $\overline{|u_{sfc}|}$ in the equilibrium state, is also about equal and fluctuates around a value of 1.6 m/s (see Table 1). These similarities can be explained by the fact that in the equatorial range, where the cloud cluster resides, all the simulations exhibit an SST of 27 ° C (see Figure 1). These considerations also confirm that $\overline{|u_{sfc}|}$ seems to be a good proxy for the circulation associated with the self-aggregation of convection.

The meridional circulation, as quantified by $\overline{|v_{sfc}|}$, develops immediately after initialization, as a result of the imposed SST contrast (Figure 5b). As expected, a stronger meridional SST contrast is associated with a stronger meridional low-level flow. The values for P_{quasi} are 3.37, 3.07, and 2.58 m/s in qobs, midqobs, and flatqobs. Even though the differences are small, in particular between qobs and midqobs, and the time series are noisy, the differences are still larger than one standard deviation. The differences may thus be seen as caused by the difference in their SST contrast rather than being a statistical artifact. Moreover, as $\overline{|u_{sfc}|}$ is independent of the SST contrast, whereas $\overline{|v_{sfc}|}$ increases with SST contrast, this analysis also explains the delayed onset of self-aggregation under stronger SST contrasts.

Finally, Figure 5b reveals that, for the equilibrium period P_{equi}, the meridional circulation is weakened. This is because the meridional circulation turns into zonal inflow at the zonal flanks of the clusters under the action of the circulation associated with the self-aggregation of convection (see Figure 2). The slow down amounts to about 13% (see Table 1).

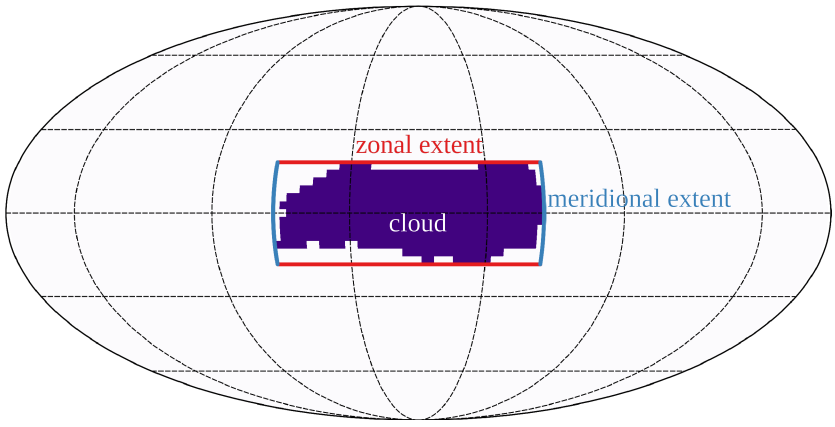

Figure 6. The schematic shows the estimation of a cloud cluster's geometrical properties, here for flatqobs at Day 60 and as used in Table 1 and Figure 7. The cluster is defined by a daily mean water vapor path exceeding 30 mm. The zonal and meridional extents are measured by the distances (km) in between maximum and minimum longitudes and latitudes, respectively. The circumference is given by the sum of the lengths of grid cell interfaces between the cloud cluster and its environment. The area fraction is the sum of the areas of grid cells within the cluster divided by the domain area. The zonal and meridional moisture fluxes (see section 3.3) are integrated along the zonal (red lines) and meridional (blue lines) extent. If more than one cluster is present, then the statistics are added.

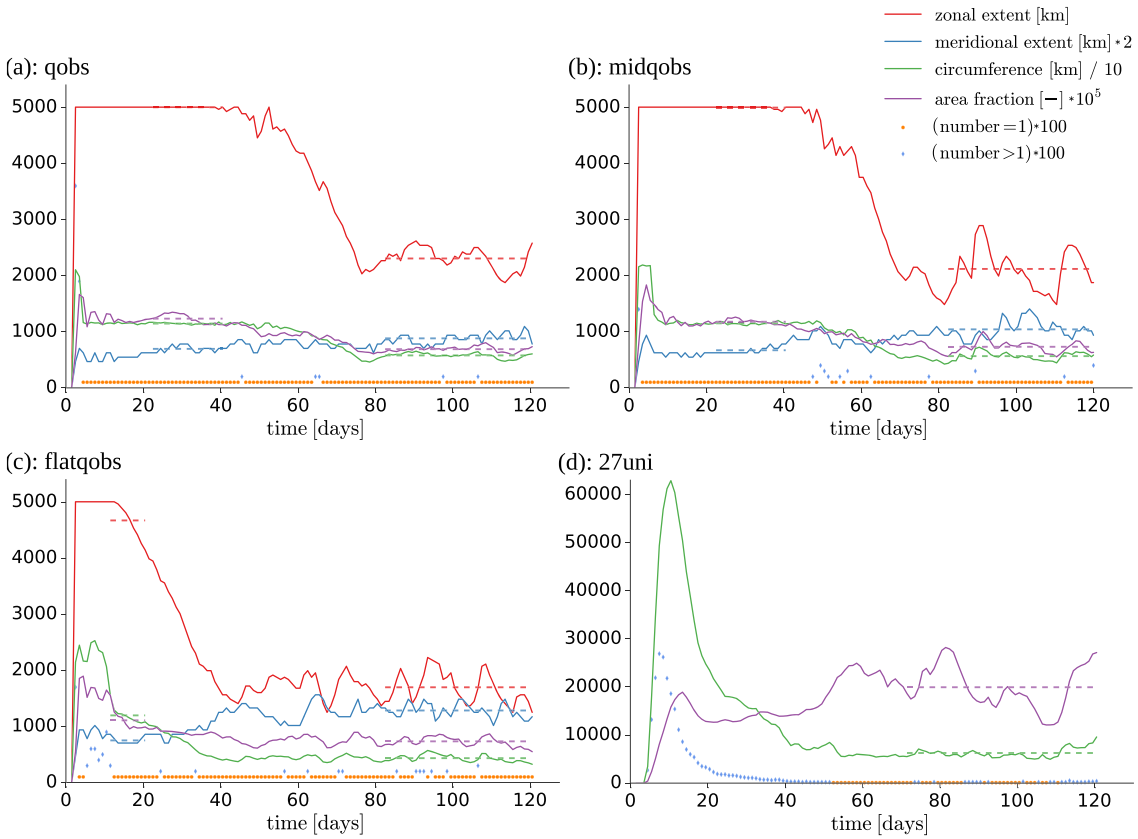

Figure 7. Temporal evolution of the geometrical properties of the cloud clusters: zonal (red) and meridional (blue) extent (km), circumference (green; km), area fraction (purple; −) and number of cloud clusters (dots; −) for (a) qobs, (b) midqobs, (c) flatqobs, and (d) 27 uni. Dashed lines denote the averages for the periods P_{quasi} and P_{equi}.

3.2.3. Aggregation Effects on the Cloud Cluster Geometry

As a final step in this section, we investigate the geometrical properties of the cloud clusters and in doing so learn about the impact of the SST contrast and of self-aggregation on the cluster geometry.

Methodologically, a grid cell is identified as part of a cloud cluster when its daily-mean water vapor path exceeds 30 mm. We found that this measure suits our purpose best, because the water vapor path is, on the one hand, a tracer of deep moist convection and, on the other hand, not too sensitive to the natural random variability of convection. It is thus smooth enough to obtain geometric properties of the cluster that are not split into many small individual clusters. The schematic in Figure 6 illustrates how the geometrical properties of a cloud cluster are estimated in more detail. In Figure 7 the zonal and meridional extents, the circumference, the fraction of area covered by cloud clusters, and the number of clusters are shown. In Table 1 the mean value and standard deviation of these properties are summarized for the quasi-equilibrium P_{quasi} and equilibrium P_{equi} periods of the simulations.

Figure 7 confirms our previous diagnostics. In 27 uni a large number of single clouds quickly develop, before merging and reducing to one cluster. The number of convective clusters, as well as their circumferences, decrease rapidly during the transient state of self-aggregation. In the three simulations with SST contrasts, we can see the breakup of the convergence line in the measure of the zonal extent. At first, it equals the domain circumference of 5,004 km, indicating that the cluster spans the entire equator. The decrease in zonal extent results from the zonal self-aggregation. The final average zonal extents of the cloud clusters in their equilibrium state P_{equi} are 2,314 2,114, and 1702 km for qobs, midqobs, and flatqobs, respectively (see Table 1). This indicates that stronger meridional SST forcing is associated with larger zonal extent. The reduction of the zonal extent by the self-aggregation of convection appears significant, and amounts to 54% in qobs, 58% in midqobs, and 66% in flatqobs between the quasi-equilibrium and equilibrium states. Also, the differences between the simulations or between the two time periods are always larger than internal variability as measured by one standard deviation (see Table 1). Finally, we recognize in Figure 7 the dependency

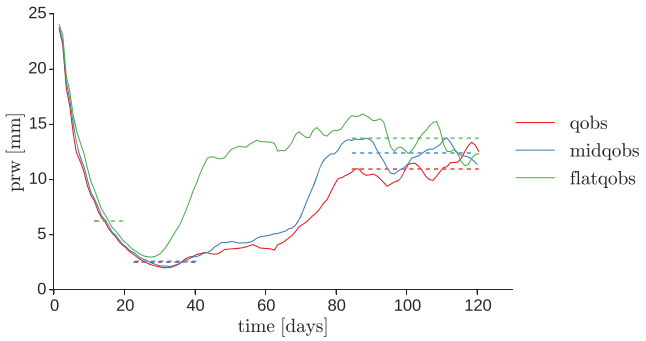

Figure 8. Temporal evolution of the daily mean of the water vapor path, averaged over regions poleward of ±45° latitude. Dashed lines denote the averages for the periods P_{quasi} and P_{equi}.

of the onset times of zonal self-aggregation on the strength of the SST contrast: the stronger the SST contrast is, the later the zonal extent decreases due to self-aggregation.

As the zonal extent decreases, the meridional extent increases. The changes are smaller than in the zonal direction: before zonal self-aggregation the meridional extent measures about 350 km for all simulations, whereas thereafter, it has expanded to 441 km for qobs, 522 km for midqobs, and 642 km for flatqobs. This means that the weaker the meridional SST forcing, the larger the meridional extent of the cloud cluster. The differences between the simulations in the P_{equi} state are not negligible, as they are larger than one standard deviation; however, they cannot be distinguished from internal variability during P_{quasi} (see Table 1).

All these results can be understood by the following considerations. It seems that for each time period, being the quasi-equilibrium state or the equilibrium state, the cluster area fraction does not depend upon the SST contrast, except in the case of uniform SST (see Table 1). The area fraction amounts to 0.12 for P_{quasi} in all three simulations with SST contrasts and 0.07 for P_{equi}. As the zonal extent does indirectly depend upon the underlying SST contrast in P_{equi}, the meridional extent has to compensate for the differences in the zonal extent between the simulations, so as to keep the cluster area fraction constant. It remains unclear why the cluster area fraction does not vary with the SST contrast. This may be related to the identical precipitation amounts, as it is known that convective area fraction tends to scale with precipitation (Davis et al., 2013; Doneaud et al., 1984). However, the precipitation amounts are also similar between the SST contrast experiments and 27 uni, despite different area fraction. Another explanation may be that convection remains confined to the same SST band in the SST contrast experiments. In fact, the average meridional extents of the cloud clusters during the equilibrium period, 441 km for qobs, 522 km for midqobs, and 642 km for flatqobs, all correspond to the band around the equator with SSTs greater than about 24.1 ° C. In other words the convection does not occur above SST colder than 24.1 ° C.

3.3. High-Latitude Moisture Budget

The interactions between forced aggregation and self-aggregation are mostly visible in the tropics. The alteration of the flow pattern by the self-aggregation of convection nevertheless has consequences for the spatial distribution of moisture, even in the high latitudes. The moistening of the high latitudes noted in section 3.1 and Figure 2 is a unique feature of our simulations and is thus investigated in more detail in this section. To understand this behavior, as in the previous section, we look at the underlying circulations. Here we mostly focus on their vertical characteristics as well as on the associated moisture transport into and out of the cloud cluster.

Figure 8 first shows the temporal evolution of the water vapor path, like in Figure 3, but only for the regions poleward of ±45°. It is evident that the high latitudes first dry drastically, when the convergence zone along the equator forms, and regain moisture when self-aggregation of convection sets in. This was observed in the convective evolution (section 3.1) and anticipated from the meridional aggregation (section 3.2; Figure 4b). The moistening in the SST contrast experiments is not symmetric around the cluster, as in 27 uni, but occurs predominantly in the meridional direction.

In Figures 9a–9c, the water vapor distribution of the temporal mean of the equilibrium state P_{equi} is shown, along with the circulation and the cloud field at three vertical levels, 0.02, 2.0, and 3.4 km. The distinct signatures of the cloud cluster and the circulation indicate that they are quasi-stationary during their 40-day equilibrium period. Also, we integrate the moisture flux for both the zonal and meridional flanks of the cloud clusters (along the purple dashed lines in Figure 9) and show their vertical profile (see Figure 9d).

At the lowest level (0.02 km) there is inflow from all directions into the cloud cluster and, associated with that, moisture import. However, between 1 and 5 km there is moisture export away from the cluster. The export happens only in the meridional direction through a meridional midlevel outflow that transports moisture to the originally dry higher latitudes. Eventually, the outflow crosses the poles. As it subsides its moisture is recycled into the cloud cluster at the zonal flanks. Here the zonal inflow layer imports moisture up to about 2.5 km, and there is no outflow in shallow to midlevels. The midlevel meridional outflow

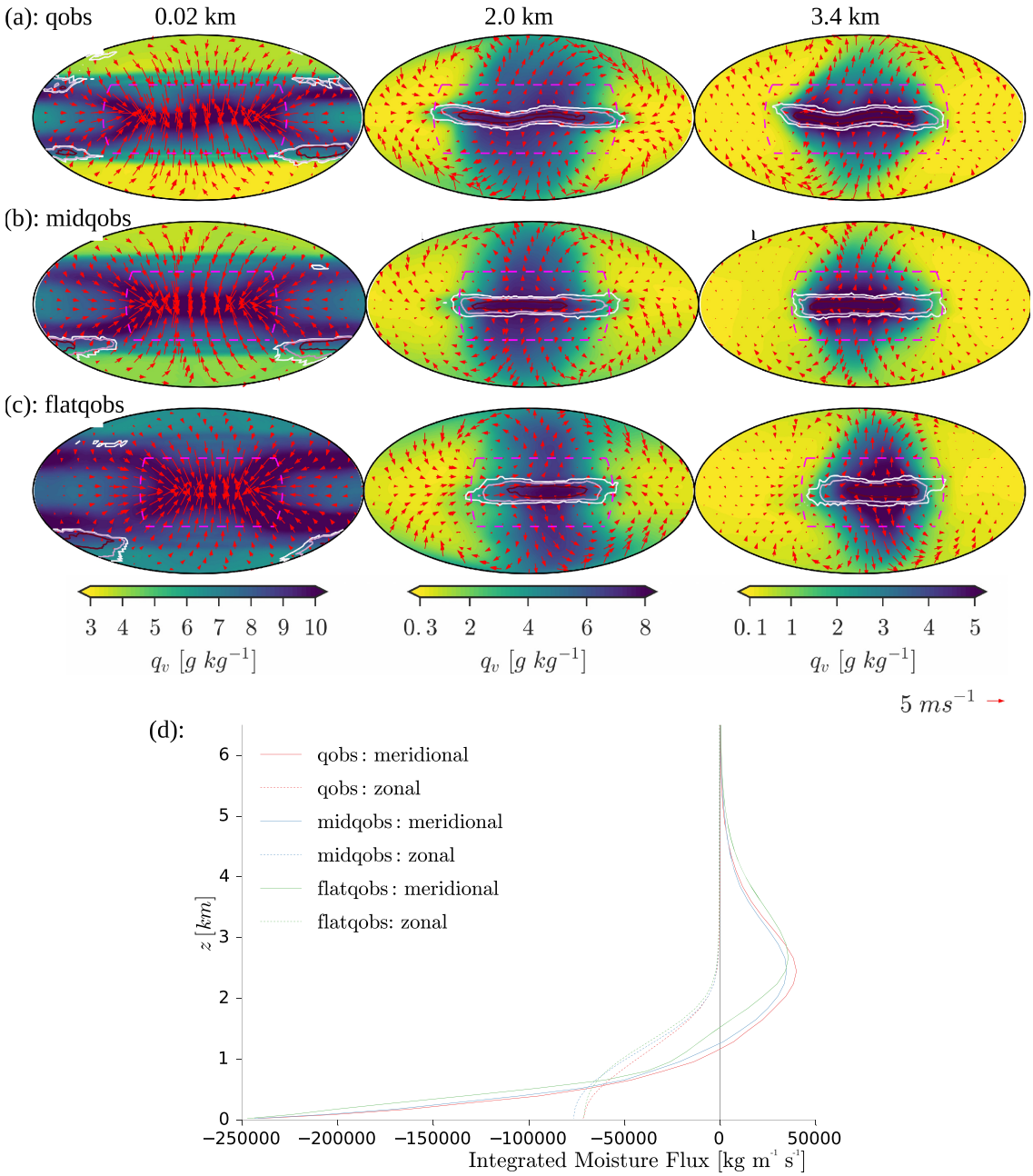

Figure 9. (a–c) Temporal average for the equilibrium period P_{equi}, at three levels, 0.02, 2.0, and 3.4 km, of the water vapor mass mixing ratio (q_v, shading; g/kg), the wind field (red arrows), and the cloud water mixing ratio (isolines of the 95th, 97th, and 99th percentile). (d) Zonal (dashed) and meridional (solid) moisture flux (kg/ms) for qobs (red), midqobs (blue), and flatqobs (green), integrated along the meridionally and zonally oriented purple dashed lines in panels (a)–(c), with import being negative and export being positive. Note that for this integration, the signs of the velocity components are chosen such that we obtain the velocity relative to the cluster, thus yielding the moisture-importing or exporting effect of the advection.

is thus responsible for the moistening of the high latitudes as well as for the increase in the domain-mean water vapor content (cf. Figure 3 with Figure 8). Note that also at high levels, there is outflow from deep convection toward the high latitudes, along with cirrus clouds, but here its effect on the moisture budget is insignificant. In topological terms we find that, at the surface level, the cluster center is an attracting node and the antipode at the equator is a repelling node. At 2 and 3.4 km, the cluster center and its antipode both look more like saddle points of the flow, and there are four gyres at ±45°, forming a global flow quadrupole.

To gain further insight into the moisture import and export, the temporal evolution of the vertically integrated moisture flux, separated into import and export, and zonal and meridional components, is shown in

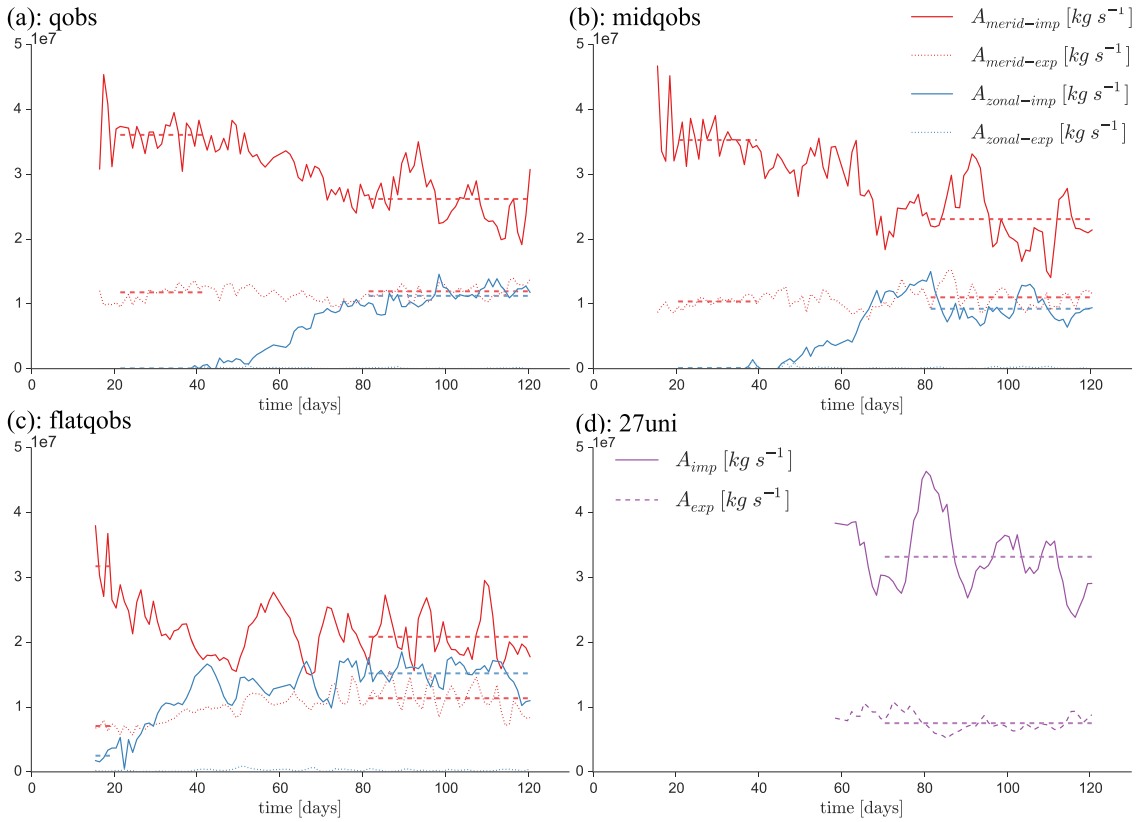

Figure 10. Temporal evolution of the vertically integrated moisture flux A, separated into meridional (red lines) and zonal contributions (blue lines), as well as into import (solid lines) and export (dashed lines) for (a) qobs, (b) midqobs, (c) flatqobs, and (d) 27 uni. For 27 uni (panel d) the distinction between zonal and meridional components is omitted, and only the period of time during which a single cloud cluster exists is considered. Dashed lines indicate the temporal averages for the periods P_{quasi} and P_{equi}.

Figure 10. For the SST contrast experiments, the meridional component of the vertically integrated moisture flux, due to the SST contrast, governs the moisture import. We also note that, with the zonal extent shrinking due to self-aggregation, the meridional moisture import weakens as well. The zonal component of the vertically integrated moisture flux contributes to the moisture import only after self-aggregation has occurred but remains at all times weaker than the meridional component. The distinct cluster geometry in the three experiments with SST contrast is also reflected in the strength of the moisture import. For instance, the zonally longer cluster in qobs imports more moisture through the meridional circulation than the zonally shorter cluster of flatqobs. In turn, the meridionally broader cluster of flatqobs imports a greater fraction of its moisture budget through the zonal circulation than the meridionally shorter cluster of qobs. These differences seem to result from the fact that although the cluster circumference and area fraction change with time, the total moisture import stays about constant and the clusters, depending upon their geometry, import moisture more through their zonal or meridional direction.

Moisture export only happens through the meridional component of the vertically integrated moisture flux, in agreement with Figure 9. The meridional moisture export is present at all times and is hardly affected by the zonal self-aggregation and by the accompanied changes of the clusters' zonal extent. Thus, the meridional outflow must intensify to export equal amounts of moisture through a shorter zonal extent, so that the integrated moisture export remains the same. This intensification results in an expansion of the meridional midlevel outflow, up to and across the high latitudes, that we identified in the temporal mean of the equilibrium period P_{equi} (see Figure 9). This fully explains the moistening of the high latitudes.

In 27 uni we find that variations in the moisture import correlate with those of the area fraction (cf. Figures 10 and 7), which suggest a close interdependency between the two: An increase in moisture import comes along with an increase in cluster area (see, e.g., around Day 80) and vice versa. The same positive correlation holds for the area fraction of precipitation as well as for the domain mean precipitation (not shown).

The ratios of moisture import to moisture export for the periods P_{quasi} and P_{equi} are given in Table 1. For the equilibrium period P_{equi} the ratios are similar across the three SST contrast simulations (3.1, 3.0, and 3.2 for qobs, midqobs, and flatqobs, respectively), but much lower than in 27 uni (4.6). This means that the elongated clusters export a greater fraction of their moisture budget than the quasi-circular cluster of 27 uni, ultimately leading to the moistening of the high latitudes. We expect that the elongation of the cloud cluster is responsible for this, although we cannot rule out the effect of the different SSTs. Likewise, the ratios tend to be smaller during P_{equi} than during P_{quasi}, although the inherent large variability prevents us from drawing firm conclusions here.

Even though our simulations do not include rotation, it is interesting to note that the intensification of the moist meridional outflow responsible for the moistening of the high latitudes exhibits some features reminiscent of atmospheric rivers (see, e.g., Newell et al., 1992; Ralph et al., 2010; Zhu & Newell, 1998). First, from Figure 9, we see that the outflow carries significant amounts of water vapor. Second, the flow's location just above the boundary layer, within altitudes of 1 to 5 km, resembles the characteristic of atmospheric rivers as low-level jets (Ralph et al., 2010). Finally, atmospheric rivers are found to be related to large-scale convergence (Waliser et al., 2012; Zhu & Newell, 1998) in the ITCZ and Kelvin waves (Ralph et al., 2010). Thus, the circulation pattern of the equilibrium period P_{equi}, as it is also characterized by low-level convergence, constitutes another analogy to atmospheric rivers.

4. Conclusions

In this study, we investigated the interactions between the aggregation of convection, as forced by spatially varying SSTs, and the self-aggregation of convection. To that aim, we used convection-permitting simulations integrated on a small aqua-planet. The setup is similar to past RCE simulations, but, instead of using homogeneous SSTs, we imposed large-scale SST contrasts in the meridional direction, following the "qobs" profile that has been used in traditional aqua-planet experiments. We control the SST profile by the value of the chosen SST contrast between 0° and 60° latitude (see equation (1)). To better understand the effect of the SST contrast on the self-aggregation of convection, we vary the strength of the contrast.

At first, a convergence line comprising of deep convection forms at the equator as a result of the SST contrast. After some time though, the convergence line breaks up and contracts zonally, as a result of the self-aggregation of convection until reaching an equilibrium state. The zonal contraction is significant and amounts between 54% and 66% depending on the strength of the tested SST contrasts. It is also accompanied by a weak meridional expansion. The strength of the SST forcing controls the stability of the (zonally oriented) convergence line as well as the geometry of the resulting cloud cluster. A stronger SST contrast leads to a later breakup of the convergence line, a smaller zonal contraction, and consequently a smaller meridional expansion. These results can be understood by the fact that a stronger SST contrast leads to a stronger meridional circulation, whereas the zonal circulation, which reflects the self-aggregation of convection, stays constant. In fact, the surface component of the meridional wind velocity in the various simulations scales with the square root of the SST difference between equator and off-equator latitudes as long as the self-aggregation has not set in.

Interestingly, it appears that, in the equilibrium state, the cluster area does not depend upon the underlying SST contrast and neither does the total moisture import into the cluster nor its export. The convection is also bound to the same SSTs, in our case the 24.1 ° C isoline. This means that changes in the zonal extent of the convective cluster, whereby the zonal extent is sensitive to the SST contrast, have to be compensated by corresponding changes in the meridional extent and that a weaker SST contrast can support a wider cloud cluster.

Furthermore, we find that the circulation of the elongated cloud cluster in the experiments with spatially varying SSTs is particularly organized. There is import of moisture below 1 km, both in the zonal and meridional direction, but export of moisture between 1–5 km only in the meridional direction. The integrated moisture import is stronger in the meridional than in the zonal direction, but the total import stays about constant in time, so that, depending on the cluster geometry and hence the SST contrast, more or less of it occurs in the meridional direction. The integrated meridional moisture export also remains constant in time. Thus, as the cloud cluster zonally contracts due to the self-aggregation and its zonal extent shrinks, the moist meridional outflow intensifies and expands. This leads to a visible moistening of the high latitudes once self-aggregation sets in. The characteristics of the moist outflow are reminiscent of atmospheric rivers.

Our study bridges the gap between traditional RCE studies and aqua-planet experiments. We focused on analyzing the interactions between forced aggregation by the imposed SST pattern and self-aggregation in terms of the resulting spatial distribution of convection, the underlying circulation, and the associated moisture transport. In particular, we took self-aggregation for granted, but it would be interesting in follow-up studies to investigate which of the self-aggregation mechanisms are at play in such a configuration. Also, it remains unclear why the simulations keep their cluster area constant, are bounded by the same SSTs, or produce similar precipitation amounts. More importantly, our study remains idealized, and it would be worth investigating which aspects apply to the real word. In particular, it is based on an idealization of observed SSTs, but given the use of a smaller radius, the SST gradients are emphasized. Key for the stability of the convergence line is nevertheless the strength of the resulting SST-driven circulation. With values of around 5 m/s close to the equator, the circulation seems to be of similar strength to circulations obtained in traditional full-Earth aqua-planet simulations. Still, it would be very interesting to test our findings using observations. Our results suggest that the ITCZ may be sensitive to the self-aggregation of convection in the zonal direction and that self-aggregation of convection acting on the ITCZ may be seen as a precursor to the formation of atmospheric rivers. More precisely our findings suggest that longer convergence lines are more likely to be found under a stronger SST contrast. More broadly, our results may explain why the ITCZ, for instance, over the tropical Atlantic, infrequently spans the whole basin.

Acknowledgments
We thank Timothy W. Cronin and an anonymous reviewer who helped to improve the manuscript significantly. Katherine Fodor and Russell Glazer are acknowledged for their careful proof-reading. This research was funded by the Max Planck Institute for Meteorology. Computations were carried out at the German Climate Computing Center (DKRZ) on the Mistral super computer. Primary data and scripts used in the analysis that may be used for reproducing the authors' work are stored in the DKRZ long term archive and can be obtained online (at https://cera-www.dkrz.de/WDCC/ui/cerasearch/entry?acronym=DKRZ_LTA_925_ds00002).

References

Back, L. E., & Bretherton, C. S. (2009). On the relationship between SST gradients, boundary layer winds, and convergence over the tropical oceans. *Journal of Climate*, *22*(15), 4182–4196.

Bechtold, P., Semane, N., & Malardel, S. (2013). Convection and waves on small planets and the real Earth. *ECMWF Newsletter*, *135*, 14–19.

Becker, T., Stevens, B., & Hohenegger, C. (2017). Imprint of the convective parameterization and sea-surface temperature on large-scale convective self-aggregation. *Journal of Advances in Modeling Earth Systems*, *9*, 1488–1505. https://doi.org/10.1002/2016MS000865

Beucler, T., Abbott, T. H., Cronin, T. W., & Pritchard, M. S. (2019). Comparing convective self-aggregation in idealized models to observed moist static energy variability near the equator. *Geophysical Research Letters*, *36*, 10,589–10,598. https://doi.org/10.1029/2019GL084130

Bony, S., Stevens, B., Frierson, D. M., Jakob, C., Kageyama, M., Pincus, R., et al. (2015). Clouds, circulation and climate sensitivity. *Nature Geoscience*, *8*(4), 261.

Bretherton, C. S., Blossey, P. N., & Khairoutdinov, M. (2005). An energy-balance analysis of deep convective self-aggregation above uniform SST. *Journal of the Atmospheric Sciences*, *62*(12), 4273–4292.

Bretherton, C. S., & Khairoutdinov, M. F. (2015). Convective self-aggregation feedbacks in near-global cloud-resolving simulations of an aquaplanet. *Journal of Advances in Modeling Earth Systems*, *7*, 1765–1787. https://doi.org/10.1002/2015MS000499

Bretherton, C. S., & Sobel, A. H. (2002). A simple model of a convectively coupled Walker circulation using the weak temperature gradient approximation. *Journal of Climate*, *15*(20), 2907–2920.

Coppin, D., & Bony, S. (2015). Physical mechanisms controlling the initiation of convective self-aggregation in a General Circulation Model. *Journal of Advances in Modeling Earth Systems*, *7*, 2060–2078. https://doi.org/10.1002/2015MS000571

Craig, G., & Mack, J. (2013). A coarsening model for self-organization of tropical convection. *Journal of Geophysical Research: Atmospheres*, *118*, 8761–8769. https://doi.org/10.1002/jgrd.50674

Davis, J., Collier, C., Davies, F., Burton, R., Pearson, G., & Di Girolamo, P. (2013). Vertical velocity observed by Doppler lidar during cops–A case study with a convective rain event. *Meteorologische Zeitschrift*, *22*(4), 463–470.

Doneaud, A., Ionescu-Niscov, S., Priegnitz, D. L., & Smith, P. L. (1984). The area-time integral as an indicator for convective rain volumes. *Journal of Climate and Applied Meteorology*, *23*(4), 555–561.

Eiras-Barca, J., Ramos, A. M., Pinto, J. G., Trigo, R. M., Liberato, M. L., & Miguez-Macho, G. (2018). The concurrence of atmospheric rivers and explosive cyclogenesis in the North Atlantic and North Pacific basins. *Earth System Dynamics*, *9*(1), 91–102.

Gimeno, L., Nieto, R., Vázquez, M., & Lavers, D. A. (2014). Atmospheric rivers: A mini-review. *Frontiers in Earth Science*, *2*, 2.

Giorgetta, M. A., Brokopf, R., Crueger, T., Esch, M., Fiedler, S., Helmert, J., et al. (2018). ICON-A, the atmosphere component of the ICON Earth System Model: I. Model description. *Journal of Advances in Modeling Earth Systems*, *10*, 1613–1637. https://doi.org/10.1029/2017MS001242

Grabowski, W. W. (2001). Coupling cloud processes with the large-scale dynamics using the cloud-resolving convection parameterization (CRCP). *Journal of the Atmospheric Sciences*, *58*(9), 978–997.

Guan, B., & Waliser, D. E. (2015). Detection of atmospheric rivers: Evaluation and application of an algorithm for global studies. *Journal of Geophysical Research: Atmospheres*, *120*, 12,514–12,535. https://doi.org/10.1002/2015JD024257

Held, I. M., Hemler, R. S., & Ramaswamy, V. (1993). Radiative-convective equilibrium with explicit two-dimensional moist convection. *Journal of the Atmospheric Sciences*, *50*(23), 3909–3927.

Hohenegger, C., & Stevens, B. (2016). Coupled radiative convective equilibrium simulations with explicit and parameterized convection. *Journal of Advances in Modeling Earth Systems*, *8*, 1468–1482. https://doi.org/10.1002/2016MS000666

Hohenegger, C., & Stevens, B. (2018). The role of the permanent wilting point in controlling the spatial distribution of precipitation. *Proceedings of the National Academy of Sciences*, *115*(22), 5692–5697.

Holloway, C. E., Wing, A. A., Bony, S., Muller, C., Masunaga, H., L'Ecuyer, T. S., et al. (2017). Observing convective aggregation. *Surveys in Geophysics*, *38*(6), 1199–1236.

Holloway, C. E., & Woolnough, S. J. (2016). The sensitivity of convective aggregation to diabatic processes in idealized radiative-convective equilibrium simulations. *Journal of Advances in Modeling Earth Systems*, *8*, 166–195. https://doi.org/10.1002/2015MS000511

Jablonowski, C., & Williamson, D. L. (2006). A baroclinic instability test case for atmospheric model dynamical cores. *Quarterly Journal of the Royal Meteorological Society*, *132*(621C), 2943–2975.

Jankov, I., Bao, J.-W., Neiman, P. J., Schultz, P. J., Yuan, H., & White, A. B. (2009). Evaluation and comparison of microphysical algorithms in ARW-WRF model simulations of atmospheric river events affecting the California coast. *Journal of Hydrometeorology*, *10*(4), 847–870.
Klemp, J., Dudhia, J., & Hassiotis, A. (2008). An upper gravity-wave absorbing layer for NWP applications. *Monthly Weather Review*, *136*(10), 3987–4004.
Lavers, D. A., Villarini, G., Allan, R. P., Wood, E. F., & Wade, A. J. (2012). The detection of atmospheric rivers in atmospheric reanalyses and their links to British winter floods and the large-scale climatic circulation. *Journal of Geophysical Research*, *117*, D20106. https://doi.org/10.1029/2012JD018027
Lindzen, R. S., & Nigam, S. (1987). On the role of sea surface temperature gradients in forcing low-level winds and convergence in the tropics. *Journal of the Atmospheric Sciences*, *44*(17), 2418–2436.
Mapes, B. (2016). Gregarious convection and radiative feedbacks in idealized worlds. *Journal of Advances in Modeling Earth Systems*, *8*, 1029–1033. https://doi.org/10.1002/2016MS000651
Mauritsen, T., & Stevens, B. (2015). Missing iris effect as a possible cause of muted hydrological change and high climate sensitivity in models. *Nature Geoscience*, *8*(5), 346.
Möbis, B., & Stevens, B. (2012). Factors controlling the position of the Intertropical Convergence Zone on an aquaplanet. *Journal of Advances in Modeling Earth Systems*, *4*, M00A04. https://doi.org/10.1029/2012MS000199
Müller, S. K. (2019). Convectively generated gravity waves and convective aggregation in numerical models of tropical dynamics (Ph.D. Thesis), Doctoral dissertation, Universität Hamburg, Hamburg. https://doi.org/10.17617/2.3025587
Muller, C., & Bony, S. (2015). What favors convective aggregation and why? *Geophysical Research Letters*, *42*, 5626–5634. https://doi.org/10.1002/2015GL064260
Muller, C. J., & Held, I. M. (2012). Detailed investigation of the self-aggregation of convection in cloud-resolving simulations. *Journal of the Atmospheric Sciences*, *69*(8), 2551–2565. https://doi.org/10.1175/JAS-D-11-0257.1
Müller, S. K., Manzini, E., Giorgetta, M., Sato, K., & Nasuno, T. (2018). Convectively generated gravity waves in high resolution models of tropical dynamics. *Journal of Advances in Modeling Earth Systems*, *10*, 2564–2588. https://doi.org/10.1029/2018MS001390
Neale, R. B., & Hoskins, B. (2000a). A standard test for AGCMs including their physical parametrizations. II: Results for the Met Office Model. *Atmospheric Science Letters*, *1*(2), 108–114
Neale, R. B., & Hoskins, B. J. (2000b). A standard test for AGCMs including their physical parametrizations: I: The proposal. *Atmospheric Science Letters*, *1*(2), 101–107.
Newell, R. E., Newell, N. E., Zhu, Y., & Scott, C. (1992). Tropospheric rivers?—A pilot study. *Geophysical research letters*, *19*(24), 2401–2404.
Nolan, D. S., Powell, S. W., Zhang, C., & Mapes, B. E. (2010). Idealized simulations of the Intertropical Convergence Zone and its multilevel flows. *Journal of the Atmospheric Sciences*, *67*(12), 4028–4053.
Popke, D., Stevens, B., & Voigt, A. (2013). Climate and climate change in a radiative-convective equilibrium version of ECHAM6. *Journal of Advances in Modeling Earth Systems*, *5*, 1–14. https://doi.org/10.1029/2012MS000191
Posselt, D. J., Heever, S. v. d., Stephens, G., & Igel, M. R. (2012). Changes in the interaction between tropical convection, radiation, and the large-scale circulation in a warming environment. *Journal of Climate*, *25*(2), 557–571.
Prein, A. F., Langhans, W., Fosser, G., Ferrone, A., Ban, N., Goergen, K., et al. (2015). A review on regional convection-permitting climate modeling: Demonstrations, prospects, and challenges. *Reviews of Geophysics*, *53*, 323–361. https://doi.org/10.1002/2014RG000475
Ralph, FMartin, Neiman, P. J., Kiladis, G. N., Weickmann, K., & Reynolds, D. W. (2010). A multi-scale observational case study of a Pacific atmospheric river exhibiting tropical-extratropical connections and a mesoscale frontal wave. *Monthly Weather Review*, *139*, 1169–1189.
Ralph, F. M., Neiman, P. J., & Wick, G. A. (2004). Satellite and CALJET aircraft observations of atmospheric rivers over the eastern North Pacific Ocean during the winter of 1997/98. *Monthly Weather Review*, *132*(7), 1721–1745.
Raymond, D. J. (1994). Convective processes and tropical atmospheric circulations. *Quarterly Journal of the Royal Meteorological Society*, *120*(520), 1431–1455.
Rotunno, R., Klemp, J. B., & Weisman, M. L. (1988). A theory for strong, long-lived squall lines. *Journal of the Atmospheric Sciences*, *45*(3), 463–485.
Swenson, E. T., Lu, J., & Straus, D. M. (2018). Resolution dependence and Rossby wave modulation of atmospheric rivers in an aquaplanet model. *Journal of Geophysical Research: Atmospheres*, *123*, 6297–6311. https://doi.org/10.1029/2017JD027899
Tobin, I., Bony, S., & Roca, R. (2012). Observational evidence for relationships between the degree of aggregation of deep convection, water vapor, surface fluxes, and radiation. *Journal of Climate*, *25*(20), 6885–6904.
Tompkins, A. M. (2001). Organization of tropical convection in low vertical wind shears: The role of water vapor. *Journal of the Atmospheric Sciences*, *58*(6), 529–545.
Tompkins, A. M. (2001a). On the relationship between tropical convection and sea surface temperature. *Journal of Climate*, *14*(5), 633–637.
Tompkins, A. M., & Craig, G. C. (1998). Radiative–convective equilibrium in a three-dimensional cloud-ensemble model. *Quarterly Journal of the Royal Meteorological Society*, *124*(550), 2073–2097.
Tompkins, A. M., & Semie, A. G. (2017). Organization of tropical convection in low vertical wind shears: Role of updraft entrainment. *Journal of Advances in Modeling Earth Systems*, *9*, 1046–1068. https://doi.org/10.1002/2016MS000802
Waliser, D. E., Moncrieff, M. W., Burridge, D., Fink, A. H., Gochis, D., Goswami, B., et al. (2012). The "year" of tropical convection (May 2008–April 2010): Climate variability and weather highlights. *Bulletin of the American Meteorological Society*, *93*(8), 1189–1218.
Wing, A. A., & Cronin, T. W. (2016). Self-aggregation of convection in long channel geometry. *Quarterly Journal of the Royal Meteorological Society*, *142*(694), 1–15.
Wing, A. A., & Emanuel, K. A. (2014). Physical mechanisms controlling self-aggregation of convection in idealized numerical modeling simulations. *Journal of Advances in Modeling Earth Systems*, *6*, 59–74. https://doi.org/10.1002/2013MS000269
Wing, A. A., Emanuel, K., Holloway, C. E., & Muller, C. (2017). Convective self-aggregation in numerical simulations: a review. *Surveys in Geophysics*, *38*(6), 1173–1197.
Wing, A. A., Reed, K. A., Satoh, M., Stevens, B., Bony, S., & Ohno, T. (2018). Radiative-convective equilibrium model intercomparison project. *Geoscientific Model Development*, *11*(2), 793.
Yang, D. (2018). Boundary layer diabatic processes, the virtual effect, and convective self-aggregation. *Journal of Advances in Modeling Earth Systems*, *10*, 2163–2176. https://doi.org/10.1029/2017MS001261
Zhu, Y., & Newell, R. E. (1998). A proposed algorithm for moisture fluxes from atmospheric rivers. *Monthly Weather Review*, *126*(3), 725–735.